MATERIALS SCIENCE

Transfer of orbital angular momentum of light to plasmonic excitations in metamaterials

T. Arikawa[1]*, T. Hiraoka[1]*, S. Morimoto[1]*, F. Blanchard[2], S. Tani[3], T. Tanaka[3], K. Sakai[4], H. Kitajima[4], K. Sasaki[4], K. Tanaka[1,3]†

The emergence of the vortex beam with orbital angular momentum (OAM) has provided intriguing possibilities to induce optical transitions beyond the framework of the electric dipole interaction. The uniqueness stems from the OAM transfer from light to material, as demonstrated in electronic transitions in atomic systems. In this study, we report on the OAM transfer to electrons in solid-state systems, which has been elusive to date. Using metamaterials (periodically textured metallic disks), we show that multipolar modes of the surface electromagnetic excitations (so-called spoof localized surface plasmons) are selectively induced by the terahertz vortex beam. Our results reveal selection rules governed by the conservation of the total angular momentum, which is confirmed by numerical simulations. The efficient transfer of light's OAM to elementary excitations in solid-state systems at room temperature opens up new possibilities of OAM manipulation.

INTRODUCTION

The nature of light-matter interaction is governed by the spatial-temporal structures of a light field and material wave functions. In the common case of the plane wave with no transverse phase structure in the long-wavelength regime, one obtains dipole selection rules, which has been successful in describing a variety of linear optical phenomena (*1*). Several efforts have been made to break the selection rules and access dark electronic states by violating the uniform phase condition using oblique irradiation or steep field gradient in a metallic nanogap (*2*, *3*). These methods simultaneously excite many modes due to the low symmetry, which is preferred for light energy harvesting. To selectively excite one particular dark mode, nonlinear optical techniques such as two-photon absorption have been used provided that strong light sources are available (*4*).

The vortex beam with the orbital angular momentum (OAM) (*5*, *6*) is a new and ideal tool for selectively exciting dipole-forbidden states by linear optical absorption. Its transverse phase is structured so that different selection rules from dipole ones are derived (*7*–*9*). The selectivity can also be understood in terms of the OAM transfer from light to material. This is clearly demonstrated by the observation of the dipole-forbidden *S* state–to–*D* state transition in the bound electron of a single trapped ion, where the electron absorbs both spin angular momentum (SAM) and OAM from the vortex beam (*10*). However, the transition probability of such a transition is very small due to the significant size mismatch between the diffraction-limited spot size of the vortex beam (~1000 nm) and the spatial extent of the electronic wave function (less than tens of nanometers) in atomic systems (*9*, *11*).

In this context, electrons in solids with extended wave functions are expected to provide an ideal platform for studying vortex light-matter interaction (*12*). For example, the giant Rydberg exciton (wave function extension of more than 2 μm) observed in the copper oxide at low temperature (1.2 K) is a promising candidate (*13*, *14*). Another example that is expected to work at room temperature is localized surface plasmons (LSPs). Recent electromagnetic field analyses predicted efficient OAM transfer from vortex beams to LSPs in a metallic disk of similar size to the diffraction-limited excitation beam (*15*). In the simulations, multipolar modes with larger angular momentums (quadrupole, hexapole, etc.) are selectively excited as a result of the OAM transfer, while Gaussian beam (plane wave) only splits positive and negative charges in an opposite direction, resulting in the dipole mode. In this study, we experimentally demonstrated this selective excitation using the spoof LSP (*16*–*18*), a low-frequency analog of LSP that exists around the surface of a periodically textured metallic disk (Fig. 1). It mimics LSP with tailor-made resonance frequencies depending on the geometric parameters of the subwavelength corrugation. By properly designing this metamaterial structure, we brought the resonance frequencies down to the terahertz (THz) frequency region, where nondestructive imaging of the near-field distribution is possible in a time-resolved manner (*19*, *20*). This allows us to unambiguously visualize characteristic near-field patterns around the corrugated disk and identify spoof LSP modes excited in the sample.

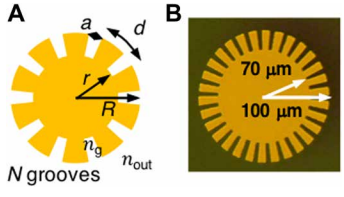

Fig. 1. Metamaterial structure for OAM transfer. (**A**) Schematic view with the following structural parameters: inner radius (*r*), outer radius (*R*), periodicity (*d*), groove width (*a*), and number of grooves (*N*). The refractive indices inside the groove and outside the disk are given by n_g and n_{out}, respectively. (**B**) Optical image of the sample made of gold ($r = 70$ μm, $R = 100$ μm, $N = 30$, and $a/d = 0.4$). The thickness is around 100 nm. Chromium (10 nm thick) is deposited under the gold as an adhesion layer.

[1]Department of Physics, Kyoto University, Kyoto 606-8502, Japan. [2]Department of Electrical Engineering, École de technologie supérieure (ÉTS), Montréal, Québec H3C 1K3, Canada. [3]Institute for Integrated Cell-Material Sciences (iCeMS), Kyoto University, Kyoto 606-8501, Japan. [4]Research Institute for Electronic Science, Hokkaido University, Hokkaido 001-0020, Japan.
*These authors contributed equally to this work.
†Corresponding author. Email: kochan@scphys.kyoto-u.ac.jp

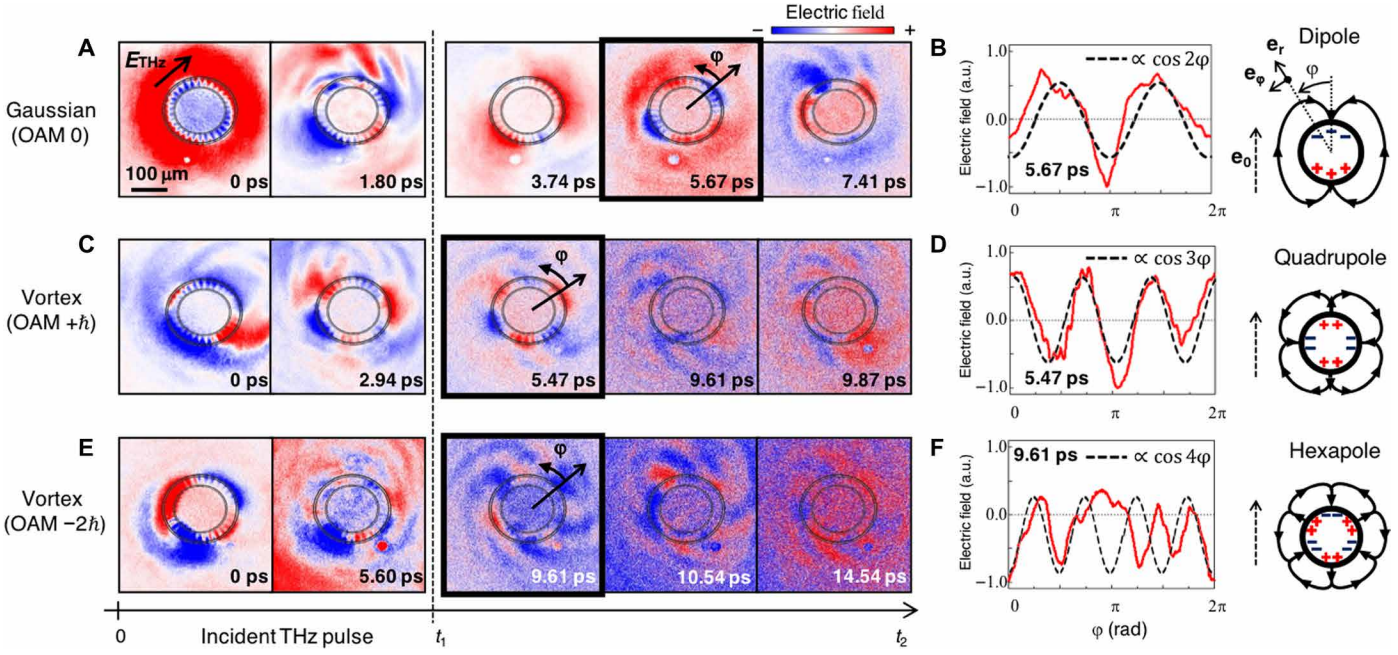

Fig. 2. Selective excitation of multipole spoof LSPs. Selected snapshots of the near-field evolution around the sample excited by (**A**) Gaussian beam, (**C**) vortex beam (OAM +ħ), and (**E**) vortex beam (OAM −2ħ). The double circle represents the position of the sample (inner and outer radius). The time origin (0 ps) is the time when the first positive peak of the incident pulse comes. The color scales are optimized at each frame for the sake of clarity. (**B**, **D**, and **F**) The electric field taken along the outer circle of the sample as a function of the azimuthal angle φ (red curves). The error bars are almost the same as the thickness of the traces. The dashed cosine curves are expected electric field patterns when the modes depicted on the right are excited. The solid arrows schematically represent the quasi-static electric field around each mode. The cosine functions are obtained by projecting the quasi-static field onto the polarization axis ($\mathbf{e_0}$, dashed up arrow) detected in the experiment. $\mathbf{e_r}$ and $\mathbf{e_\varphi}$ are cylindrical unit vectors introduced to calculate quasi-static fields (see Materials and Methods). a.u., arbitrary units.

RESULTS AND DISCUSSION

Time-resolved near-field imaging

To visualize the near-field pattern due to spoof LSPs, we fabricated corrugated gold disks directly on the top surface of the THz detector crystal (see Materials and Methods and fig. S1). This allows us to sample electric field only a few micrometers (much less than the wavelength of a few hundred micrometers) away from the metallic structure (*19*, *20*). The Gaussian and vortex excitation beams (propagating in the *z* direction) are characterized in the Supplementary Materials (figs. S2 and S3 and movies S1 to S3). We performed all the measurements at room temperature (295 K). Figure 2A shows five snapshots of the THz electric field around the sample excited by a linearly polarized Gaussian beam (movie S4). Even after the incident THz pulse has passed through the sample, an electric field oscillation localized around the outer circle of the sample is observed (third to fifth frame), which indicates a resonant excitation of a spoof LSP. It has four nodes at fixed points along the outer circle. This is shown by the red curve in Fig. 2B, where we plot the electric field taken along the outer circle of the sample at 5.67 ps (fourth frame) as a function of the azimuthal angle φ. Notice that the selected snapshots (third to fifth frame) display almost one oscillation period. These results show that a standing wave mode with a period of 4.2 ps (0.24 THz) is excited. The red curve in Fig. 2B nicely follows cos(2φ) drawn by the dashed black curve. This represents the expected electric field pattern when the dipole mode is excited in the sample, which is obtained by projecting the quasi-static electric field around the dipole onto the detection polarization axis ($\mathbf{e_0}$) in the experiment (see Materials and Methods for the relation between the charge and electric field distribution). This confirms that the dipole mode is excited by the Gaussian beam.

Figure 2C shows selected near-field images of the sample excited by a linearly polarized vortex beam with the *z* component of the OAM +ħ. A localized electric field with six zero-crossing points along the outer circle is seen after the excitation. An azimuthal plot along the outer circle at 5.47 ps (third frame) agrees excellently with cos(3φ) curve, which is the expected functional form when the quadrupole mode exists (Fig. 2D) (see Materials and Methods). Furthermore, in contrast to the Gaussian beam excitation, we can see that this electric field pattern travels along the outer circle in a clockwise direction (movie S5). This means that the quadrupolar charge distribution rotates along the φ direction and carries angular momentum. As shown in Materials and Methods, the quadrupole mode corresponds to the LSP with a traveling surface charge distribution $\rho(\varphi, t) \propto \cos(+2\varphi - 2\pi ft)$, where *f* and *t* represent frequency and time, respectively. This mode possesses the *z* component of the angular momentum of +2ħ, which means that, in addition to the SAM (+ħ from the left circularly polarized component of the linear polarization), the OAM (+ħ) of light is transferred. A similar experiment and analysis were carried out for the vortex beam excitation with the OAM −2ħ (Fig. 2, E and F, and movie S6). Although not clear as above, multipolar field pattern with eight zero-crossing points can be recognized, which partly follows the cos(4φ) curve, suggesting the excitation of the hexapole mode with the angular momentum of −3ħ [surface charge distribution $\rho(\varphi, t) \propto \cos(-3\varphi - 2\pi ft)$] (see Materials and Methods). This indicates the transfer of both SAM (−ħ from the right circularly polarized component of the linear

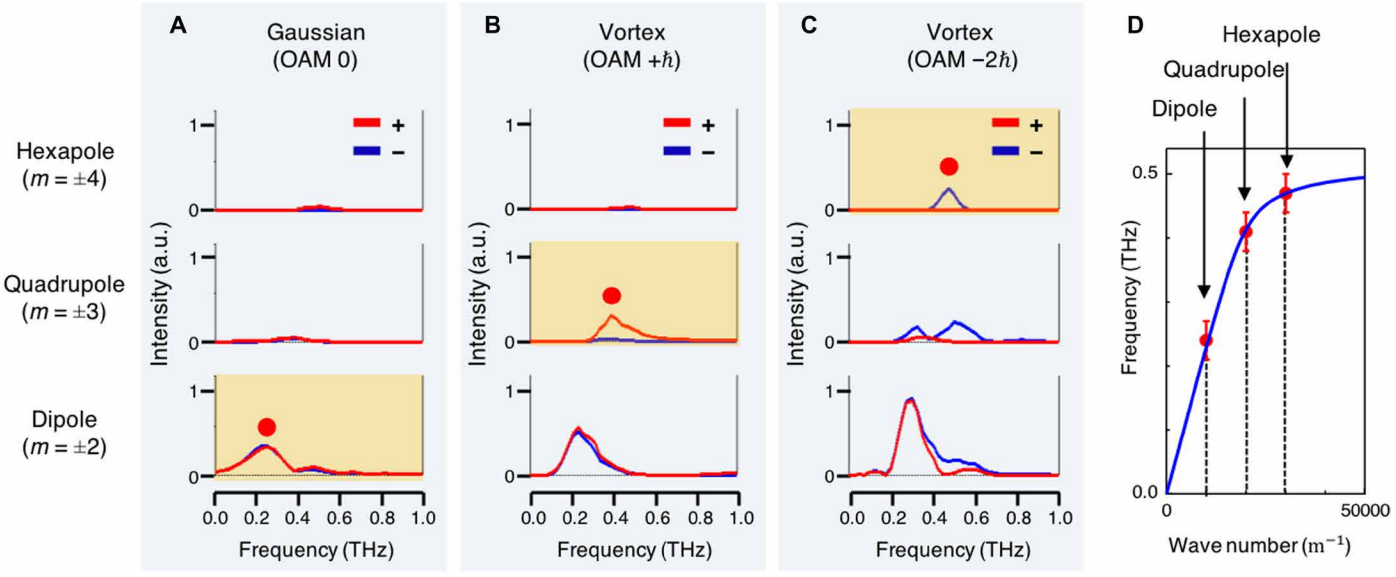

Fig. 3. Mode decomposition of near-field distributions. Frequency spectra of the dipole [$E(\pm2, f)$], quadrupole [$E(\pm3, f)$], and hexapole [$E(\pm4, f)$] modes excited in the sample illuminated by (**A**) Gaussian beam, (**B**) vortex beam ($+\hbar$), and (**C**) vortex beam ($-2\hbar$). (**D**) Dispersion relation of the spoof LSP. The red dots represent the resonance frequencies determined in (A) to (C). The blue curve is a theoretical fitting.

polarization) and OAM ($-2\hbar$). The complicated field pattern in Fig. 2F that deviates from the simple cos(4φ) function is due to the simultaneously excited dipolar and quadrupolar modes as revealed in the analysis shown below.

Mode expansion analysis

These observations indicate that multipole spoof LSPs are excited by vortex beams. To clearly illustrate this point, we performed the following analysis. The orthogonal functional forms of the electric field [cos(mφ), m: integer] for different LSP modes allow us to decompose the complicated field pattern into the superposition of each mode (see Materials and Methods). For this purpose, we focused on the electric field along the outer circle of the sample as we have done in Fig. 2 (B, D, and F), but this time including the time dependence [E(φ, t)]. We expanded E(φ, t) along both axes by two-dimensional (2D) Fourier transform to obtain $E(m,f)=\int_0^{2\pi} d\varphi \int_{t_1}^{t_2} dt E(\varphi,t)\cos(m\varphi - 2\pi f t)$. $E(m, f)$ then represents the frequency spectrum of each LSP mode (m = ±2, dipole; m = ±3, quadrupole; and so on). The positive (negative) sign of m corresponds to the traveling wave mode in the clockwise (counterclockwise) direction. To exclusively analyze the electric field generated by spoof LSPs, we only used data after the incident THz pulses have passed through the sample (t_1 to t_2 in Fig. 2). This enables us to minimize spurious signals due to the electric field of the excitation pulse (see the Supplementary Materials).

Figure 3A shows the frequency spectra of the dipole [$E(\pm2, f)$], quadrupole [$E(\pm3, f)$], and hexapole mode [$E(\pm4, f)$] in the case of the Gaussian beam excitation. We can see that only the dipole modes are excited at 0.24 THz. Note that both traveling modes with clockwise and counterclockwise directions are equally excited, which is consistent with the standing wave observed in Fig. 2A. In contrast, the frequency spectra in the case of the vortex beam ($+\hbar$) excitation show a peak in the quadrupole mode (Fig. 3B, middle) with comparable efficiency to the dipole mode. Furthermore, the positive index mode (red) is selectively excited as inferred from the clockwise traveling wave observed in Fig. 2C. Figure 3B also shows that the dipole modes are excited. This is due to the residual Gaussian beam component around 0.24 THz, which is out of the conversion range of spiral phase plate (SPP)−1 (fig. S3B). The same analysis for the case of the vortex beam ($-2\hbar$) excitation clearly demonstrates the selective excitation of the negative hexapole mode (Fig. 3C, top). The selection of the inverse rotation modes is also confirmed by inverting the sign of the OAM (fig. S4). These results demonstrate the selective and efficient excitation of the multipolar modes using the OAM of light. Note that, in Fig. 3C, dipole and negative quadrupole modes are also excited. This is explained by the Gaussian and vortex ($-\hbar$) beam components in the excitation pulse, respectively (fig. S3B, SPP-2). The characteristic structures (e.g., double peak in the quadrupole mode) come from the spectral shape of the excitation pulse. Although the simultaneous excitation of those modes complicates the electric field pattern in the time domain (Fig. 2, C and E), this analysis allows us to identify all spoof LSP modes excited in the sample.

This analysis also reveals the resonance frequencies of each mode and allows us to draw the dispersion relation (Fig. 3D). As the number of poles increases, the resonance frequency becomes higher and shows a signature of saturation, which is well reproduced by the theory (see Materials and Methods). The dispersion relation of the spoof LSPs depends on the geometrical parameters of the metallic structure. This provides a powerful tool to control the resonance frequencies. We performed similar experiments and analyses on samples with different dimensions of the corrugation and demonstrated resonance frequency control in the Supplementary Materials (figs. S5 and S6).

Selection rules

These results allow us to deduce the selection rules for the excitation of multipole spoof LSPs. Table 1 summarizes the z component of the angular momentum of the excitation beams and the observed

Table 1. Selection rules. The orbital (first row), spin (second row), and total (third row) angular momentums of the excitation beams are summarized. The last row shows the angular momentums of the spoof LSPs observed in the experiment.

	Gaussian beam	Vortex beam		Vortex beam	
OAM	0	$+\hbar$		$-2\hbar$	
SAM	$+\hbar$ and $-\hbar$	$+\hbar$ and $-\hbar$		$+\hbar$ and $-\hbar$	
TAM	$+\hbar$ and $-\hbar$	$+2\hbar$	0	$-3\hbar$	$-\hbar$
Spoof LSP	Dipole ($+\hbar$ and $-\hbar$)	Quadrupole ($+2\hbar$)		Hexapole ($-3\hbar$)	Dipole ($-\hbar$)

LSPs. Let us first revisit the excitation of the dipole mode by the uniform electric field of the Gaussian beam in terms of the angular momentum. The linearly polarized incident light is a superposition of two circularly polarized waves with the SAM of $+\hbar$ and $-\hbar$. Because of the zero OAM, the total angular momentum (TAM) is equal to the SAM. The excited dipole mode, which mimics the dipole LSP with a traveling surface charge distribution $\rho(\varphi, t) \propto \cos(\pm\varphi - 2\pi ft)$, also possesses the z component of the angular momentum of $\pm\hbar$. This gives us an alternative way to interpret the selective excitation of the dipole mode by the Gaussian beam, i.e., transfer of the TAM (= SAM) of light to the electronic system. Similar arguments hold true for the vortex beam excitations. The TAM of the linearly polarized vortex beam (OAM $+\hbar$) is $+2\hbar$ and 0. The clockwise quadrupole mode observed in the experiment also has the angular momentum of $+2\hbar$, which suggests the transfer of the TAM. Note that no LSP mode is excited by the vortex beam with the TAM of 0 (*15*). The TAM of the linearly polarized vortex beam (OAM $-2\hbar$) is $-3\hbar$ and $-\hbar$. The selective excitation of the counterclockwise hexapole mode with the angular momentum of $-3\hbar$ obeys the same rule. This rule also predicts that the field component with the TAM of $-\hbar$ at 0.5 THz should excite the counterclockwise dipole mode. This is observed in Fig. 3C (bottom) where the higher frequency tail of the counterclockwise dipole mode (blue) is stronger than the other (red). These experimental observations strongly support the selection rules governed by the conservation of the TAM. This tells us that the spoof LSP mimics not only the dispersion relation of the LSP but also the selection rules for excitation (*15*). This point is numerically confirmed from similar electromagnetic field analyses as (*15*) for spoof LSPs (see the Supplementary Materials and fig. S7).

Conclusion

The observation of the traveling surface wave indicates that the electron scattering in the sample is low enough to ensure the coherent collective motion of electrons over the entire sample. The frequency tunability by geometric designs makes the corrugated metallic disk a very versatile OAM receiver in a wide range of frequencies as long as the scattering is sufficiently low. OAM transfer to other elementary excitations in solids such as Rydberg excitons (*13*, *14*), phonons (*21*), and skyrmions (*22*) is also expected, although focusing techniques of OAM light beyond the diffraction limit (*23*, *24*) should be necessary in some cases. The efficient OAM exchange between light and elementary excitations in solid-state systems will form the foundation of novel solid-state devices for OAM applications (*25*–*27*).

MATERIALS AND METHODS

Experimental setup for THz near-field imaging

Figure S1 (A and B) schematically shows the experimental setup. We used a mode-locked Ti:Sapphire regenerative amplifier (Solstice, Spectra-Physics) that delivers 100-fs optical pulses (center wavelength, 780 nm) with 3.2-mJ pulse energy at 1-kHz repetition rate. Linearly polarized coherent THz pulses with Gaussian beam profile were generated by optical rectification in a $LiNbO_3$ (LN) crystal using tilted-pulse-front excitation scheme (fig. S1C) (*28*, *29*). Two lenses (lens 1: Tsurupica lens, $f = 50$ mm; lens 2: 3-mm-thick, 2-mm-radius silicon bullet lens) were used to match the spot size of the excitation beam to the size of the metallic structure for efficient excitation. We used 1-μm-thick x-cut LN mounted on a glass substrate as an electro-optic (EO) crystal to detect an electric field of THz pulses (*30*). 2D EO imaging was performed using a probe beam with a large spot size (*19*). The image of the probe beam at the EO crystal was relayed to a 16-bit complementary metal-oxide semiconductor camera from PCO (model pco.edge) with a polarization analyzer unit. To perform EO sampling in the reflection geometry, the top and bottom surfaces of this substrate are coated with high-reflection (HR) and anti-reflection (AR) films (3 μm thick) for the probe pulse at 780 nm, respectively. The short pass (SP) and long pass (LP) filters were used to enhance the detection sensitivity using the probe spectrum filtering technique (*20*). An x-cut LN with a thickness of 2 μm is used to compensate for the birefringence of the EO crystal. When performing vortex beam experiments, we put an SPP in the collimated part of the THz beam propagating in the z direction (*31*–*33*). We made two SPPs to generate vortex beams with the z component of the OAM of $\pm\hbar$ or $\pm2\hbar$ centered at around 0.5 THz (SPP-1 and SPP-2). We used ZEONEX (cyclo-olefin polymer; refractive index, 1.52) as a material. SPP-1 is nominally designed to convert the Gaussian beam into the vortex beam ($\pm\hbar$) at 0.45 THz. The step height is 1.29 mm. SPP-2 has a step of 2.18 mm, which generates the vortex beam ($\pm2\hbar$) at 0.53 THz. The total step heights shown above are discretized to 16 small steps. The sign of the OAM can be inverted by reversing the SPP in the beam path.

Sample fabrication

Corrugated gold disks are fabricated on the top surface (high-reflection coating material) of the THz detector crystal by a standard photolithographic technique. Chromium (10 nm thick) is deposited under the gold as an adhesion layer.

Azimuthal angle dependence of the local electric field around multipolar LSPs

As schematically shown in Fig. 2 (B, D, and F), the surface charge distributions of LSPs along the circumference (radius $r = r_0$) can be expressed as follows

$$\rho_l(\varphi) \propto \cos(l\varphi) \tag{1}$$

Here, $l = 1, 2, \ldots$ corresponds to the dipole, quadrupole, and higher-order LSPs, respectively. We ignore the time dependence (rotation of the charge distribution) at this moment and calculate the static electric field, $\mathbf{E}_l(r, \varphi)$. The scalar potential $\Phi(r, \varphi)$ can be obtained by solving the Laplace equation (at $r \neq r_0$) in cylindrical coordinates (r, φ, z). Because of the cosine-type charge distribution, the scalar potential is an even function about φ. We first consider

the 2D case. When the scalar potential is independent of z, the general solution is

$$\Phi(r,\varphi) = A_0 + B_0 \log r + \sum_{l=1}^{\infty}(A'_l r^l + A_l r^{-l})\cos(l\varphi) \quad (2)$$

where A_0, B_0, A_l, and A'_l are coefficients determined by boundary conditions. To avoid the divergence of the electric field in the limit of $r \to 0$ and $r \to \infty$, the electric field distributions have to take the following forms

$$\mathbf{E}(r,\varphi) = \begin{cases} \sum_{l=1}^{\infty} l A'_l r^{l-1}[-\cos(l\varphi)\mathbf{e_r} + \sin(l\varphi)\mathbf{e_\varphi}] \ (r \le r_0) \\ \sum_{l=1}^{\infty} l A_l r^{-l-1}[\cos(l\varphi)\mathbf{e_r} + \sin(l\varphi)\mathbf{e_\varphi}] - \frac{B_0}{r}\mathbf{e_r} \ (r \ge r_0) \end{cases} \quad (3)$$

From the boundary condition, $[\mathbf{E}(r \ge r_0, \varphi) - \mathbf{E}(r \le r_0, \varphi)]\cdot\mathbf{e_r} = \rho_l(\varphi)$ at $r = r_0$, we obtain the following result for the static electric field around $\rho_l(\varphi)$,

$$\mathbf{E}_l(r,\varphi) = l A_l r^{-l-1}[\cos(l\varphi)\mathbf{e_r} + \sin(l\varphi)\mathbf{e_\varphi}] \ (r \ge r_0) \quad (4)$$

By taking the projection onto the detection polarization axis $\mathbf{e_0} = \mathbf{e_r}\cos(\varphi) - \mathbf{e_\varphi}\sin(\varphi)$, the azimuthal angle dependence of the electric field detected in the experiment is

$$\mathbf{E}_l(\varphi)\cdot\mathbf{e}_0 \propto \cos[(l+1)\varphi] \quad (5)$$

When $\rho_l(\varphi)$ rotates as $\rho_l(\varphi, t) = \cos(l\varphi \mp 2\pi f t) = \cos(\pm l\varphi - 2\pi f t)$, additional electric field components such as radiation field and induced field are generated. However, in the near-field regime, the following quasi-static field is the dominant one

$$E_l(\varphi, t) \propto \cos[\pm(l+1)\varphi - 2\pi f t] \quad (6)$$

By replacing $\pm(l+1)$ by $m = \pm 2$ (dipole), ± 3 (quadrupole), and so on, we have

$$E_m(\varphi, t) \propto \cos[m\varphi - 2\pi f t] \quad (7)$$

This shows that different LSP modes correspond one-to-one to cosine functions that are orthogonal to each other. Similar calculation for $l = 0$, i.e., a uniform surface charge $\rho_0(\varphi) \propto$ const., leads to the following form

$$E_1(\varphi, t) \propto \cos(\varphi)\cos(2\pi f t) \quad (8)$$

These functions $E_m(\varphi, t)$ ($m = \pm 1, \pm 2, \pm 3, \ldots$) plus $E_0(\varphi, t) =$ const. form a complete set for symmetric field distributions about $\varphi = 0$ with the period of 2π. In the actual 3D case (100-nm-thick disk), the electric field distribution starts to deviate from the simple cosine functions (Eq. 7), as the detection plane gets away from the center of the sample along the z direction. In our experiment, this effect is minimized by measuring the electric field distribution in the plane as close to the sample as possible. Therefore, we assumed that the electric field distribution can be approximately expressed by Eq. 7 and performed the mode expansion analysis. The effectiveness of this approximation is supported by the excellent agreement between the frequency spectrum obtained from the experimental data (based on the 2D model) and the numerical simulation (full 3D) shown in the Supplementary Materials (fig. S7).

Dispersion relation of spoof LSPs

The dispersion relation of the spoof surface plasmons that propagate on the periodically corrugated metal surfaces is given as follows (*34*, *35*)

$$k = \frac{2\pi f n_{\text{out}}}{c}\sqrt{1 + \left(\frac{a}{d}\frac{n_{\text{out}}}{n_{\text{g}}}\right)^2 \tan^2\left(\frac{2\pi f n_{\text{g}}}{c}(R - r)\right)} \quad (9)$$

Here, k is the wave vector along the surface and c is the speed of light. The asymptotic (cutoff) frequency in the limit of $k \to \infty$ is $c/4n_{\text{g}}(R - r)$. By folding the surface to make a corrugated metallic disk, k becomes the wave vector along the circumference, which is quantized because of the periodic boundary condition. We used Eq. 9 as a fitting function in Fig. 3D. The fitting parameters determined by the method of least squares are $n_{\text{g}} = 4.8$ and $n_{\text{out}} = 2.1$. These numbers represent the effective refractive indices for the electromagnetic waves inside the groove and outside the disk. These should be expressed by combinations of the refractive indices of air ($n = 1.00$), silicon ($n = 3.41$), glass ($n = 1.96$), high-reflection coating materials ($n \sim 2$), and LN ($n = 5.11$) with appropriate weightings depending on the spatial extent of the electric field (see fig. S1B for the structure around the metallic disk). The high effective index inside the groove ($n_{\text{g}} = 4.8$) indicates that the electromagnetic mode is strongly localized around the LN ($n = 5.11$). The effective index outside the disk ($n_{\text{out}} = 2.1$), which is close to the index of the glass substrate ($n = 1.96$), suggests that the localization is weaker.

SUPPLEMENTARY MATERIALS

Supplementary material for this article is available at http://advances.sciencemag.org/cgi/content/full/6/24/eaay1977/DC1

REFERENCES AND NOTES

1. M. Fox, *Optical Properties of Solids* (Oxford Univ. Press, ed. 2, 2010).
2. F. Hao, E. M. Larsson, T. A. Ali, D. S. Sutherland, P. Nordlander, Shedding light on dark plasmons in gold nanorings. *Chem. Phys. Lett.* **458**, 262–266 (2008).
3. M. Takase, H. Ajiki, Y. Mizumoto, K. Komeda, M. Nara, H. Nabika, S. Yasuda, H. Ishihara, K. Murakoshi, Selection-rule breakdown in plasmon-induced electronic excitation of an isolated single-walled carbon nanotube. *Nat. Photonics* **7**, 550–554 (2013).
4. R. Boyd, *Nonlinear Optics* (Academic Press, ed. 3, 2008).
5. L. Allen, M. W. Beijersbergen, R. J. C. Spreeuw, J. P. Woerdman, Orbital angular momentum of light and the transformation of Laguerre-Gaussian laser modes. *Phys. Rev. A* **45**, 8185–8189 (1992).
6. S. Franke-Arnold, Optical angular momentum and atoms. *Philos. Trans. A Math Phys. Eng. Sci.* **375**, 20150435 (2017).
7. S. J. Van Enk, G. Nienhuis, Commutation rules and eigenvalues of spin and orbital angular momentum of radiation fields. *J. Mod. Opt.* **41**, 963–977 (1994).
8. M. F. Andersen, C. Ryu, P. Cladé, V. Natarajan, A. Vaziri, K. Helmerson, W. D. Phillips, Quantized rotation of atoms from photons with orbital angular momentum. *Phys. Rev. Lett.* **97**, 170406 (2006).
9. C. T. Schmiegelow, F. Schmidt-Kaler, Light with orbital angular momentum interacting with trapped ions. *Eur. Phys. J. D* **66**, 157 (2012).
10. C. T. Schmiegelow, J. Schulz, H. Kaufmann, T. Ruster, U. G. Poschinger, F. Schmidt-Kaler, Transfer of optical orbital angular momentum to a bound electron. *Nat. Commun.* **7**, 12998 (2016).
11. A. Alexandrescu, D. Cojoc, E. Di Fabrizio, Mechanism of angular momentum exchange between molecules and Laguerre-Gaussian beams. *Phys. Rev. Lett.* **96**, 243001 (2006).
12. K. Shigematsu, K. Yamane, R. Morita, Y. Toda, Coherent dynamics of exciton orbital angular momentum transferred by optical vortex pulses. *Phys. Rev. B* **93**, 045205 (2016).
13. T. Kazimierczuk, D. Fröhlich, S. Scheel, H. Stolz, M. Bayer, Giant Rydberg excitons in the copper oxide Cu_2O. *Nature* **514**, 343–347 (2014).
14. A. M. Konzelmann, S. O. Krüger, H. Giessen, Interaction of orbital angular momentum light with Rydberg excitons: Modifying dipole selection rules. *Phys. Rev. B* **100**, 115308 (2019).
15. K. Sakai, K. Nomura, T. Yamamoto, K. Sasaki, Excitation of multipole plasmons by optical vortex beams. *Sci. Rep.* **5**, 8431 (2015).
16. A. Pors, E. Moreno, L. M. Moreno, J. B. Pendry, F. J. G. Vidal, Localized spoof plasmons arise while texturing closed surfaces. *Phys. Rev. Lett.* **108**, 223905 (2012).

17. X. Shen, T. J. Cui, Ultrathin plasmonic metamaterial for spoof localized surface plasmons. *Laser Photonics Rev.* **8**, 137–145 (2014).
18. L. Chen, Y. Wei, X. Zang, Y. Zhu, S. Zhuang, Excitation of dark multipolar plasmonic resonances at terahertz frequencies. *Sci. Rep.* **6**, 22027 (2016).
19. F. Blanchard, A. Doi, T. Tanaka, H. Hirori, H. Tanaka, Y. Kadoya, K. Tanaka, Real-time terahertz near-field microscope. *Opt. Express* **19**, 8277–8284 (2011).
20. F. Blanchard, K. Tanaka, Improving time and space resolution in electro-optic sampling for near-field terahertz imaging. *Opt. Lett.* **41**, 4645–4648 (2016).
21. L. Zhang, Q. Niu, Chiral phonons at high-symmetry points in monolayer hexagonal lattices. *Phys. Rev. Lett.* **115**, 115502 (2015).
22. H. Fujita, M. Sato, Ultrafast generation of skyrmionic defects with vortex beams: Printing laser profiles on magnets. *Phys. Rev. B* **95**, 054421 (2017).
23. T. Arikawa, S. Morimoto, K. Tanaka, Focusing light with orbital angular momentum by circular array antenna. *Opt. Express* **25**, 13728–13735 (2017).
24. K. Sakai, T. Yamamoto, K. Sasaki, Nanofocusing of structured light for quadrupolar light-matter interactions. *Sci. Rep.* **8**, 7746 (2018).
25. N. Bozinovic, Y. Yue, Y. Ren, M. Tur, P. Kristensen, H. Huang, A. E. Willner, S. Ramachandran, Terabit-scale orbital angular momentum mode division multiplexing in fibers. *Science* **340**, 1545–1548 (2013).
26. A. Nicolas, L. Veissier, L. Giner, E. Giacobino, D. Maxein, J. Laurat, A quantum memory for orbital angular momentum photonic qubits. *Nat. Photonics* **8**, 234–238 (2014).
27. H. Ren, X. Li, Q. Zhang, M. Gu, On-chip noninterference angular momentum multiplexing of broadband light. *Science* **352**, 805–809 (2016).
28. J. Hebling, G. Almási, I. Kozma, J. Kuhl, Velocity matching by pulse front tilting for large area THz-pulse generation. *Opt. Express* **10**, 1161–1166 (2002).
29. H. Hirori, A. Doi, F. Blanchard, K. Tanaka, Single-cycle terahertz pulses with amplitudes exceeding 1 MV/cm generated by optical rectification in $LiNbO_3$. *Appl. Phys. Lett.* **98**, 091106 (2011).
30. C. Winnewisser, P. U. Jepsen, M. Schall, V. Schyja, H. Helm, Electro-optic detection of THz radiation in $LiTaO_3$, $LiNbO_3$ and ZnTe. *Appl. Phys. Lett.* **70**, 3069 (1997).
31. M. W. Beijersbergen, R. P. C. Coerwinkel, M. Kristensen, J. P. Woerdman, Helical-wavefront laser beams produced with a spiral phaseplate. *Opt. Commun.* **112**, 321–327 (1994).
32. G. A. Turnbull, D. A. Robertson, G. M. Smith, L. Allen, M. J. Padgett, The generation of free-space Laguerre-Gaussian modes at millimetre-wave frequencies by use of a spiral phaseplate. *Opt. Commun.* **127**, 183–188 (1996).
33. K. Miyamoto, K. Suizu, T. Akiba, T. Omatsu, Direct observation of the topological charge of a terahertz vortex beam generated by a Tsurupica spiral phase plate. *Appl. Phys. Lett.* **104**, 261104 (2014).
34. F. J. Garcia-Vidal, L. Martín-Moreno, J. B. Pendry, Surfaces with holes in them: New plasmonic metamaterials. *J. Opt. A Pure Appl. Opt.* **7**, S97–S101 (2005).
35. A. Rusina, M. Durach, M. I. Stockman, Theory of spoof plasmons in real metals. *Appl. Phys. A* **2**, 375–378 (2010).

Acknowledgments
Funding: This work was supported by JSPS KAKENHI (26247052, 17H06124, 16K17529, and 19K05306), JST CREST, and JST ACCEL (JPMJMI17F2). This work was supported in part by Kyoto University Nanotechnology Hub in "Nanotechnology Platform Project" sponsored by the Ministry of Education, Culture, Sports, Science and Technology (MEXT), Japan. **Author contributions:** T.H. and S.M performed the measurements and analyzed the data under the supervision and guidance of T.A., F.B., and K.T. S.T. and T.T. helped initial measurements and data analysis. K. Sakai, H.K., and K. Sasaki performed numerical simulations. T.A. and K.T. prepared the manuscript. All authors discussed the results and contributed to the manuscript. **Competing interests:** The authors declare that they have no competing interests. **Data and materials availability:** All data needed to evaluate the conclusions in the paper are present in the paper and/or the Supplementary Materials. Additional data related to this paper may be requested from the authors.

Submitted 28 May 2019
Accepted 1 May 2020
Published 12 June 2020
10.1126/sciadv.aay1977

Citation: T. Arikawa, T. Hiraoka, S. Morimoto, F. Blanchard, S. Tani, T. Tanaka, K. Sakai, H. Kitajima, K. Sasaki, K. Tanaka, Transfer of orbital angular momentum of light to plasmonic excitations in metamaterials. *Sci. Adv.* **6**, eaay1977 (2020).

Transfer of orbital angular momentum of light to plasmonic excitations in metamaterials

T. Arikawa, T. Hiraoka, S. Morimoto, F. Blanchard, S. Tani, T. Tanaka, K. Sakai, H. Kitajima, K. Sasaki and K. Tanaka

Sci Adv **6** (24), eaay1977.
DOI: 10.1126/sciadv.aay1977